JJEE
Volume 11 | Number 1 | March 2025 | Pages 151-167

Jordan Journal of Electrical Engineering

ISSN (print): 2409-9600, ISSN (online): 2409-9619

Homepage: jjee.ttu.edu.jo

Multi-Objective Optimization of SEPIC-Cuk Converter for Photovoltaic Application

Minyahil Tanashu[1*], Tassew Tadiwos[2], Amare Kassaw[3], Seifu Admasu[4], Getasew Admasu[5], Noah Ezra[6], Teng Long[7], Lara Allen[8], Elizabeth M. Tennyson[9], Sam Stranks[10], Tefera Terefe[11]

[1, 2, 3, 4, 5] Bahir Dar University, Bahir Dar Institute of Technology, Bahir Dar, Ethiopia
E-mail: tanashuminyahil@gmail.com
[6, 7] University of Cambridge, Department of Engineering, UK
[8, 9] Centre for Global Equality, Cambridge, UK
[10] Department of Physics, Cavendish Laboratory, University of Cambridge, UK
[11] Adama Science and Technology University, EPCE, Adama, Ethiopia

Received: Jul 26, 2024 *Revised: Sep 20, 2024* *Accepted: Sep 30, 2024* *Available online: Oct 15, 2024*

***Abstract*—** This paper investigates the optimization of SEPIC-Cuk DC-DC converters to enhance efficiency and compactness, addressing the increasing demands of modern power converters. Given the topological structure, a paralleling approach is crucial due to its potential to improve both size and performance. Utilizing a bipolar SEPIC-Cuk configuration, this research meticulously evaluates, refines, and validates an experimental prototype of a bipolar DC-DC converter. To achieve optimal outcomes, the investigation employs a multi-objective metaheuristic optimization technique, focusing on efficiency and size attributes to design a cost-effective converter. The selection of design parameters - including switching frequency, capacitance, inductance, and power electronic switches - is integral to the optimization process. The proposed converter features a single switch control mechanism to operate a single input and dual output structure, ensuring high efficiency while enhancing converter response and minimizing ripple. A laboratory prototype of a low-cost 300 W converter, designed for a bipolar DC microgrid as a photovoltaic optimizer, has been developed and tested, accommodating an input voltage range of 20 V to 60 V and supporting standard output voltages. Experimental results demonstrate an average efficiency of 97.5% and 98.35% for a 300 W load, validating the effectiveness of the proposed strategy. Additionally, a comprehensive comparison between theoretical predictions and experimental findings is presented, confirming the validity and applicability of the proposed methodology.

***Keywords*—** DC-DC converter optimization; SEPIC-Cuk converter; Efficiency analysis; Volume analysis; Inductor design; Photovoltaics.

1. INTRODUCTION

DC-DC converters play a crucial role in photovoltaic (PV) systems by enhancing efficiency and increasing voltage gain. A study referenced in [1] introduced a high-gain SEPIC converter equipped with a grey wolf-optimized PI controller, which significantly improved system efficiency and reduced losses in PV applications. Similarly, research in [2] focused on the state-space modeling and design of DC-DC converters, highlighting the importance of capacitors in optimizing performance. A proposed zero-voltage-switching (ZVS) full-bridge cascaded step-up DC-DC converter, featuring a resonant auxiliary circuit, was designed for high voltage-gain applications [3]. Other studies have developed converters aimed at efficient power transfer, including a high-gain DC-DC converter for solar PV applications [4], an isolated switched-boost converter [5], and a high-power quality boost converter [6]. Additionally,

* Corresponding author
DOI: https://doi.org/10.5455/jjee.204-1722004077

innovative designs such as a wide input voltage DC-DC converter [7] and a high voltage-gain common-ground three-port DC-DC converter [8] have been introduced to meet diverse solar energy needs. A single-switch inductor-coupled DC-DC converter was also designed for fault diagnosis in PV systems [9-11]. These advancements collectively aim to optimize power transfer, voltage regulation, and overall system efficiency in solar energy applications. Reason: Improved vocabulary, clarity, and technical accuracy while correcting grammatical and punctuation errors.

The research presented in [12] introduced an optimized PID controller for a DC-DC buck converter utilizing the Archimedes Optimization Algorithm (AOA). This study demonstrated the AOA's effectiveness in fine-tuning the PID controller for superior closed-loop performance, surpassing the results of controllers adjusted using alternative methods such as the hybrid Nelder-Mead method, artificial ecosystem-based optimization, differential evolution, and particle swarm optimization. In contrast, [13] proposed an optimized DC-DC converter employing a modified switched inductor-capacitor technique to achieve ultra-high voltage gain, particularly for renewable energy applications. This converter exhibited enhanced performance in terms of voltage gain and efficiency by integrating a modified switched inductor cell interleaved with the main switch. Research in [14] introduced a non-isolated, ultra-high voltage-gain coupled inductor-based DC-DC converter, demonstrating its capability to achieve significantly higher output voltages without the need for isolation. Furthermore, [15] explored the application of advanced control techniques, such as fuzzy logic controllers, to enhance the performance of non-isolated DC-DC converters.

Traditional solar power systems depend on expensive and bulky transformers, which can lead to inefficiencies. However, grounding without transformers is possible through a combined Cuk-SEPIC (CCS) topology, utilizing a streamlined DC-AC inverter for residential mains. A Common DC Bus system is more efficient and simpler than traditional AC systems, facilitating quicker interconnections and reducing costs. To ensure consistent utilization of solar power, Distributed DC-DC converters (Micro DC-DC) are installed at each photovoltaic (PV) panel, offering precise control, as illustrated in Fig. 1.

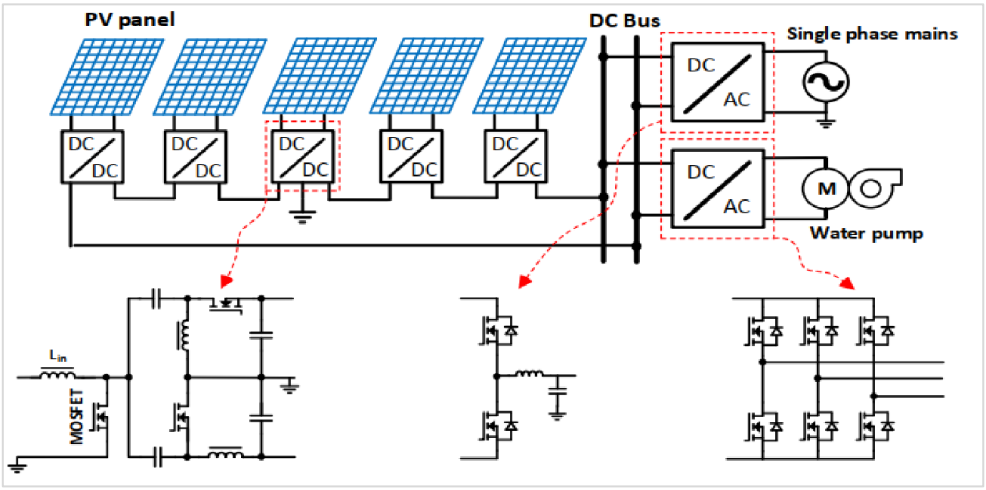

Fig. 1. The DC bus system.

This paper proposes a combined Cuk-SEPIC-based micro-DC-DC converter system to manage low granularity and ensure optimal DC solar irrigation and power supply for communities. By utilizing modular DC-AC full-bridge inverters, the system reduces costs and

complexity on the load side, leveraging a common DC bus for both irrigation and solar power applications. Additionally, the system enhances reliability and resilience through fault ride-through and plug-and-play capabilities, creating a custom modular solution tailored to the needs of farmers. When integrating pumps into the system, it is essential to consider factors such as the size and type of water sources, water quality, and storage tank requirements. This research develops a modular and expandable DC bus system that is compatible with micro-DC-DC converters, with design optimization achieved through genetic algorithms. This approach improves interconnection and modularity, enabling the development of efficient, low-cost pump drives and power supplies. Current solar irrigation pumps are often prohibitively expensive and overly powerful for small farms. This work aims to implement modern methods that minimize costs and losses while achieving high efficiency and power density.

The paper contributes to the field of DC-DC converter design by introducing a prototype of a Single Input Multiple Output (SIMO) DC-DC converter that employs a SEPIC-Cuk topology. This innovative design effectively generates multiple output voltages from a single input. A key advancement is the simplification achieved by utilizing only one controlled switch, managed by a microcontroller with a grounded control terminal. This approach reduces complexity compared to traditional topologies that require multiple switches, streamlining the design process and enhancing reliability. Additionally, the paper compares the SEPIC-Cuk topology with conventional SEPIC and Cuk converters, highlighting its advantages, such as a smaller volume, reduced losses, and the resolution of the floating nature of photovoltaic (PV) output. These benefits underscore the potential of the SEPIC-Cuk topology for practical applications in microgrids and distributed power systems, offering a more efficient and compact solution for power management in DC microgrids.

2. LITERATURE REVIEW

DC microgrids are increasingly favored over AC microgrids due to their lower wiring requirements, higher efficiency, and reduced electromagnetic interference [16]. Despite challenges such as flexible load management and complex protection systems, DC microgrids are well-suited for large distributed generation systems [17]. Bipolar networks, although intricate, provide advantages including improved power control, reduced losses, and enhanced system resilience through the independent operation of outputs [18]. The robust nature of bipolar DC microgrids ensures their reliability for power distribution and management [19]. Integrating a SEPIC-Cuk converter with distributed generation into bipolar DC microgrids facilitates balanced dual-output voltage using a single switching device.

DC-DC converters are crucial components in power electronic systems, particularly in electric vehicles, renewable energy applications, and distributed resources. Recent studies have investigated various optimization strategies to enhance efficiency, power density, reliability, and cost-effectiveness. For instance, a comparison of topologies utilizing discrete inductors and an Interphase Transformer demonstrated that new multi-phase, high-power bi-directional converters can achieve significant improvements in power density and efficiency [20]. Geometric modeling of polynomial functions has enabled the rapid generation of optimal designs for multi-level converters [21]. Additionally, metaheuristic optimization techniques, such as the Earthquake Algorithm and the BAT algorithm, have advanced inductance selection and PI controller optimization in buck converters [22, 23].

Research has also focused on optimizing inductors to enhance efficiency and power density. Techniques such as particle swarm optimization have been employed to maximize the quality factor of integrated spiral inductors [24]. Comparisons between discrete inductors and interphase transformers have provided valuable insights for high-power bi-directional DC-DC converters [25].

Metaheuristic methods, including ant colony optimization and differential evolution, have been utilized in the design of CMOS RF square spiral inductors [26]. The optimization of inductors in a buck or boost converters using genetic algorithms has resulted in improved size and loss parameters [27]. In the context of electric vehicles, optimized bi-directional DC-DC converters have achieved competitive power density and efficiency, with outputs reaching 4 kW/L and 7 kW/kg [28].

Optimizing DC-DC converters for photovoltaic (PV) applications is essential for maximizing energy efficiency and output. Techniques such as multi-objective optimization have been employed to address various performance criteria, including maximum power point tracking (MPPT) mechanisms for grid-connected PV systems [29].

Approaches like NSGA-II have enhanced the compactness and efficiency of DC-DC boost converters in two-stage AC-DC power supplies [30]. Additionally, adaptive fuzzy logic controllers and dynamic optimization algorithms have been utilized to customize optimization strategies for high step-up DC-DC converters in solar PV systems [31, 32].

Furthermore, optimization techniques have been applied to SiC-based DC-DC converters in electric vehicles [33] and phase-shift modulation in DC grid interface converters [34]. These studies highlight the critical importance of optimization in advancing DC-DC converter technology across various applications, particularly in renewable energy systems.

3. MATERIALS AND METHODS

3.1. Circuit Operation and Design Overview

The circuit topology consists of two switches connected in parallel and two diodes also connected in parallel to enhance power handling capability while controlling the output voltage through complementary switching, as illustrated in the circuit diagram in Fig. 2. The proposed converter circuit diagram is shown in Fig. 2a.

In Mode 1, when switch S (parallel) is ON and diodes D1 (parallel) and D2 (parallel) are OFF, the input inductor (L1) is charged by the input current (is), while the SEPIC capacitor (C1) discharges its energy into inductor L2. Meanwhile, the Cuk capacitor (C2) charges as its stored energy is transferred to the Cuk inductor (L3) due to the higher input voltage, as depicted in Fig. 2b. In Mode 2, when switch S is OFF and diodes D1 and D2 are ON, the energy stored in inductor L1 is transferred to both capacitors C1 and C2, resulting in a decrease in the input current (is). Simultaneously, inductors L2 and L3 discharge their stored energy to their respective capacitors (C01 and C02), supplying power to the load. This operation is characterized by efficient energy management and transfer between the inductors and capacitors, particularly in Continuous Conduction Mode (CCM), as illustrated in Fig. 2c.

The converter functions in two modes: continuous conduction mode (CCM), where the inductor current remains continuous, and discontinuous conduction mode (DCM), where the current drops to zero briefly during the switching cycle. Controlled sources can be used to analyze the converter's steady-state behavior as shown in Fig. 3.

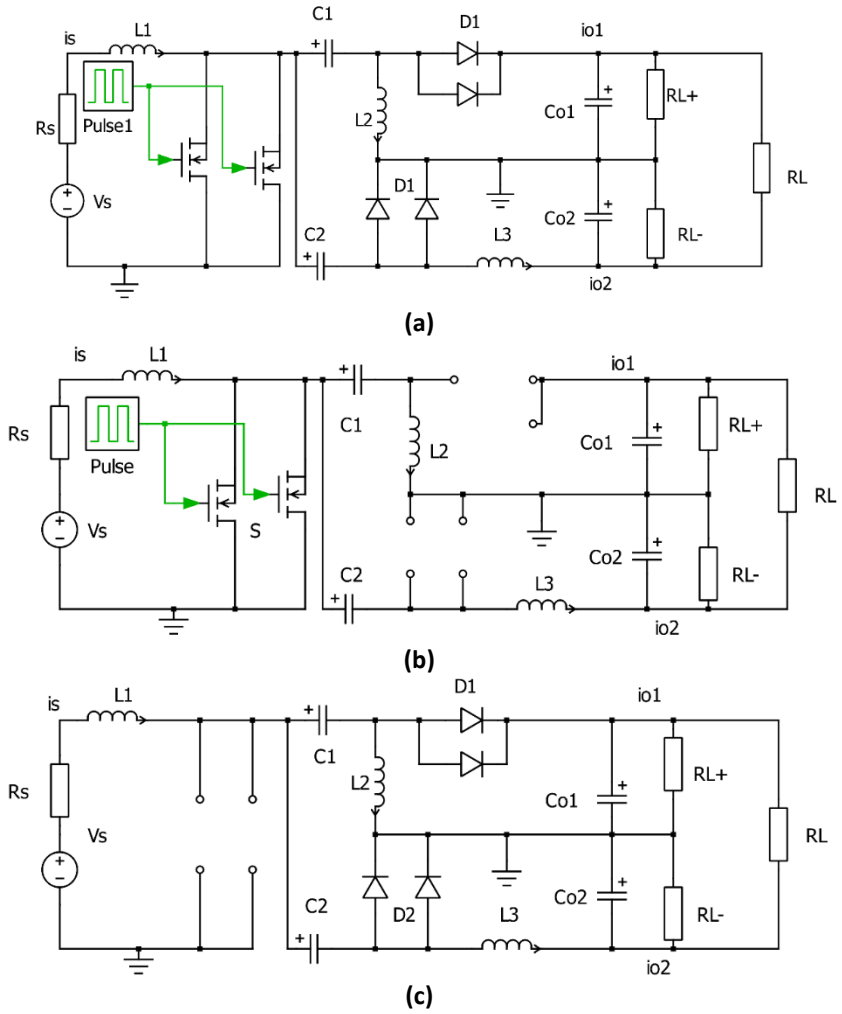

Fig. 2. The proposed converter: a) circuit diagram; b) mode 1 (switch S is on, D_1 and D_2 are off); c) mode 2 (switch S is off, D_1 and D_2 are on).

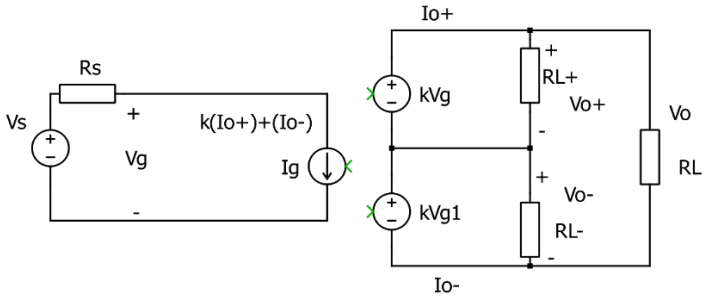

Fig. 3. Converter's steady-state model.

The transfer parameter k is influenced by the converter's operating mode. When the converter is in continuous conduction mode (CCM), k should be:

$$k = \frac{D}{1-D} \tag{1}$$

where D is the duty cycle. In the case of discontinuous conduction mode (DCM), the value of k is given by the expression [35].

$$k = D\sqrt{\frac{R_o T_s}{2L_{eq}}} \tag{2}$$

where T_S is the switching period, R_o is resistance and L_{eq} inductance. At the maximum power point $R_s = R_g$. R_g is the equivalent resistance at the load terminal. The input current is given by

$$I_g = k^2 V_g [\frac{1}{R_L^+} + \frac{1}{R_L^-} + \frac{4}{R_L}] \quad (3)$$

where V_g is the output voltage. For a balanced bipolar grid of voltage ± V_{dc}, at the positive output, the power can be expressed by:

$$P^+ = \frac{V_g^{\,2}}{2R_s} = V_{dc} I_o^+ \quad (4)$$

So, from the circuit I_o^+ can be established as

$$I_o^+ = \frac{2kV_g - V_{dc}}{2k^2 R_s} = \frac{V_g^{\,2}}{2V_{dc} R_s} \quad (5)$$

Thus, k is determined by the voltage at the converter's input V_s and the output voltage V_o of the photovoltaic system at its maximum power point. The duty ratio expression is as:

$$D_{\min} = \frac{V_o + V_{fwd}}{V_S + V_o + V_{fwd}} \quad (6)$$

$$D_{\max} = \frac{V_o + V_{fwd}}{V_S + V_o + V_{fwd}} \quad (7)$$

where V_{fwd} = forward voltage drops of the diode. The maximum duty ratio D_{max} and minimum duty ratio D_{min} occur at a minimum and maximum input voltage.

Voltage stress of the switch

$$V_g + V_o^+ \quad (8)$$

Voltage stress of diode D_1

$$V_g + V_o^+ \quad (9)$$

Voltage stress of diode D_1

$$V_g + V_o^- \quad (10)$$

Average Current across the switch

$$I_{sw} = \frac{V_g D^2}{R_L (1-D)^2} \quad (11)$$

Average Current across for diode D_1

$$I_{D1} = \frac{V_g D^2}{R_L^+ (1-D)^2} \quad (12)$$

Average Current across for diode D_2

$$I_{D2} = \frac{V_g D^2}{R_L^- (1-D)^2} \quad (13)$$

The selection of the L_1 inductor depends on the desired ripple value of the input current. Its peak-to-peak value is given by

$$L_1 = \frac{V_{g(\min)} D_{\max}}{\Delta i_{L1} f_{sw}} \quad (14)$$

Δi_{L1} is a percentage of the input current average. For the choice of the inductors $L_1 = L_2 = L_3$. it is assumed that the converter works in CCM in a power range.

The expression for peak current $I_{L(pk)}$ flowing through these inductors is,

$$I_{L1(pk)} = \frac{I_s}{\eta} + \frac{\Delta I_L}{2} \tag{15}$$

$$I_{L3(pk)} = I_{o2} + \frac{\Delta I_L}{2} \tag{16}$$

$$I_{L2(pk)} = I_{o1(\max)} + \frac{\Delta I_L}{2} \tag{17}$$

On the other hand, the combination of SEPIC and Cuk converters works in CCM when the following expression is satisfied:

$$\frac{2L_{eq}}{R_L T_s} > (1-D)^2 \tag{18}$$

The selection of the link capacitors C_1 and C_2, for the SEPIC and Cuk sides is given as:

SEPIC side

$$C_1 = \frac{V_{o1} D}{R_L^{+} f_{sw} \Delta Vc_1} \tag{19}$$

Cuk side

$$C_2 = \frac{V_{o1} D}{R_L^{-} f_{sw} \Delta Vc_2} \tag{20}$$

In the same way, the voltage ripple in C_1 and C_2 is given by:

$$\Delta Vc_1 = \frac{D^2 V_g}{(1-D) R_L^{+} C_1 f_s} \Rightarrow \frac{\Delta Vc_1}{V_{o1}} = \frac{D}{R_L^{+} C_1 f_s} \tag{21}$$

$$\Delta Vc_2 = \frac{D^2 V_g}{(1-D) R_L^{-} C_1 f_s} \Rightarrow \frac{\Delta Vc_1}{V_{o2}} = \frac{D}{R_L^{-} C_1 f_s} \tag{22}$$

The selection of the output capacitors C_{o1} and C_{o2} is also made to obtain the desired voltage ripple value. Its peak-to-peak value is given by:

$$\frac{\Delta Vc_1}{V_{01}} = \frac{D}{R_o^{+} C f_s} \tag{23}$$

$$\frac{\Delta Vc_1}{V_{02}} = \frac{D}{R_o^{-} C f_s} \tag{24}$$

$$C_{02} = C_{01} = \frac{V_{01/02} D_{\max}}{R_L^{-/+} C f_s} \tag{25}$$

The design specification parameters are described as shown in Table 1.

Table 1. Design specifications of the proposed converter.

Converter parameter	Value
Input voltage range	20-30 V
Rated power	300 W
Rated current	10 A
Supported output voltage	12 V/24 V/36 V/ 48V

3.2. Inductor Optimization

To determine the magnetic flux density at any point in the core to find a residual function of B [36] as:

$$F\left(B\right)=B-\mu\left(B,k\right)H \tag{26}$$

The above statement can be formulated as per Ampere's Law:

$$F(B)=B-\mu_o\frac{r(B,k)}{r(B,k)-1}\frac{NI_c}{2\pi r} \tag{27}$$

The toroid's center origin is represented by the radius in cylindrical coordinates from the coil, I_c being the current applied.

$$\lambda_m(I_c)=\frac{Nl_c}{2}\sum_{n=1}^{N_p-1}(r_{n+1}-r_n)(B_{n+1}(I_c)+B_n(I_c)) \tag{28}$$

The energy stored in the winding region can be used to determine the permeance of leakage in a specific area.

$$E=PN^2\frac{i^2}{2} \tag{29}$$

$$E=\frac{1}{2}\mu\int_v H^2dV \tag{30}$$

P is the permeation connected to energy (E), N is each turn counted, and i is current. The coil's geometry provides information about ohmic losses. The DC resistance can be found as:

$$R_{dc}=\frac{V_{cl}N^2}{k_{pf}A^2{}_{cl}\delta(T)} \tag{31}$$

$$k_{pf}=\frac{A_{cd}}{A_{ci}} \tag{32}$$

where σ(T) is the conductivity of copper at a given temperature and N is the number of turns, pdf is the packing factor, A_{cd} is the conductor cross-section. A_{cl} is coil cross-section area, and V_{cl} is volume. The proximity losses can be computed as:

$$P_{p,x}=\frac{\overline{dl}^2}{dt}\left(\frac{\mu_o N^3\pi\delta(T_x)r^4{}_s l_x P_{lk,x}}{4V_{cl,x}}\right) \tag{33}$$

where, l_x is the length of such section of coil x, and $P_{lk,x}$ each region. The inductor optimization problem can be formulated as:

$$\min_y\left[P_L\ M_L\right] \tag{34}$$

Subject to $\begin{aligned}&Maximum\ wire\ length\ \le\ 3m\\&Maximum\ packing\ factor\le\ 0.75\\&Maximum\ aspect\ ratio\le\ 8\\&Maximum\ weight\le\ 0.3Kg\\&Maximum\ power\ loss\le\ 3\text{W}\\&Maximum\ winding\ temperature\le\ 130^oC\end{aligned}$

where PL represents the total losses (including core, proximity, and AC winding losses), the design space of the inductor is defined as y = [N, a*, ra, lc, dc]. Here, N denotes the number of turns, a* represents the conductor area, ra is the inner radius of the core, and lc is the axial

length of the core, which is used to determine the shape of the device and calculate its mass ML. The fitness function is designed to minimize both mass and losses in the inductor, provided that all criteria are satisfied. Table 2 describes the parameters of the inductor for optimization.

Table 2. Inductor parameters.

Parameter	Value
Minimum number of coils turns	20
Maximum desired conductor area	1.025 mm^2
Minimum inner radius	9.71 mm
Maximum the axial length	25 mm
Peak current	10 A
Operating frequency	100 kHz
Ambient temperature	30 ^{o}C
Winding built factor	0.9
Maximum achievable permeability	100
Heat transfer coefficient winding to air	2 W/m^{2}K
Protection layer heat transfer coefficient	560 W/m^{2}K

Fig. 4a illustrates the relative permeability profile of the inductor core, depicting the spatial distribution of relative permeability from a top view. Fig. 4b presents the flux density profile within the inductor core. The yellow regions indicate areas of higher flux density, where the magnetic field is stronger, while the lighter regions correspond to lower flux density, represented as blue areas.

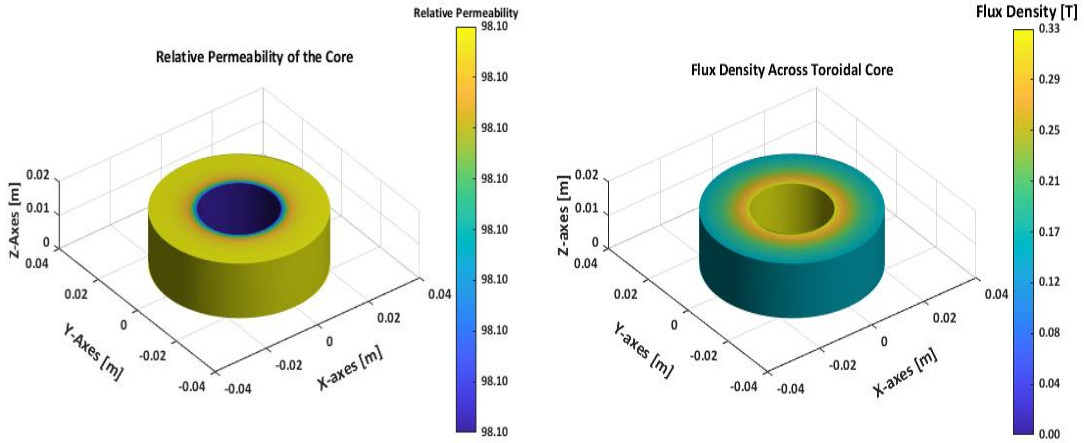

(a) **(b)**

Fig. 4. Profile of the core: a) relative permeability; b) flux density.

Fig. 5a illustrates the profiles of relative permeability and flux density as a function of the radial distance from the center of the inductor core. The relative permeability curve (in blue) indicates that the permeability of the core material varies slightly with radial position. This non-uniform distribution of permeability influences how the magnetic flux is concentrated and directed within the core. The flux density is highest in the yellow region, where the relative permeability also reaches its maximum. Fig. 5b presents data on the field energy stored in the inductor and the peak current applied through the winding. The field energy stored in the inductor core is 0.005944 J, representing the amount of energy magnetically stored within the core when the inductor is energized.

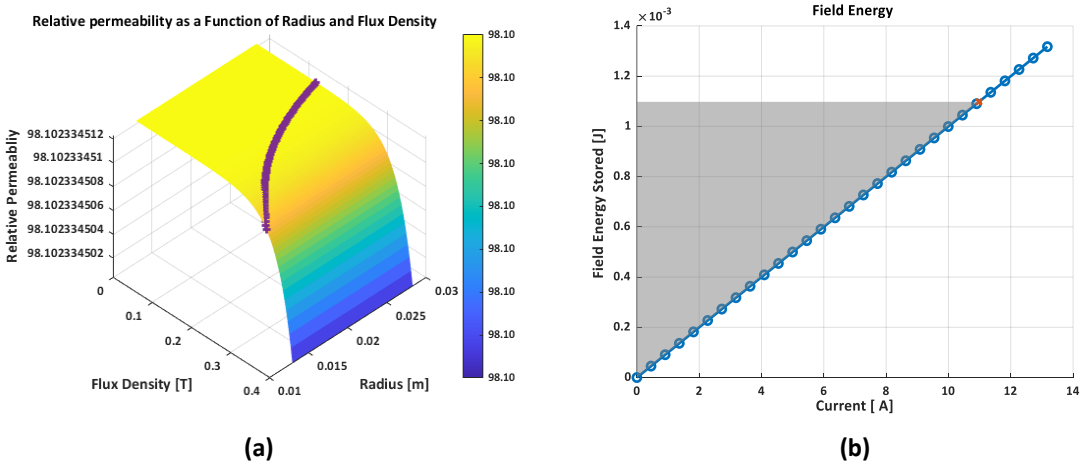

Fig. 5. Profile of the core as a function of the radial distance from the center of the inductor core: a) Relative permeability; b) flux density

Fig. 6a illustrates the relationship between the temperature of the inductor and its total mass. The graph demonstrates a positive correlation between inductor mass and maximum operating temperature. The slope of the line indicates the rate at which the maximum temperature increases with inductor mass. Fig. 6b presents the Pareto optimal front of inductors, taking into account their volume, mass, and power loss. The Pareto optimal front represents a set of inductor designs that exemplify the best trade-offs among these three parameters, as shown in Table 3.

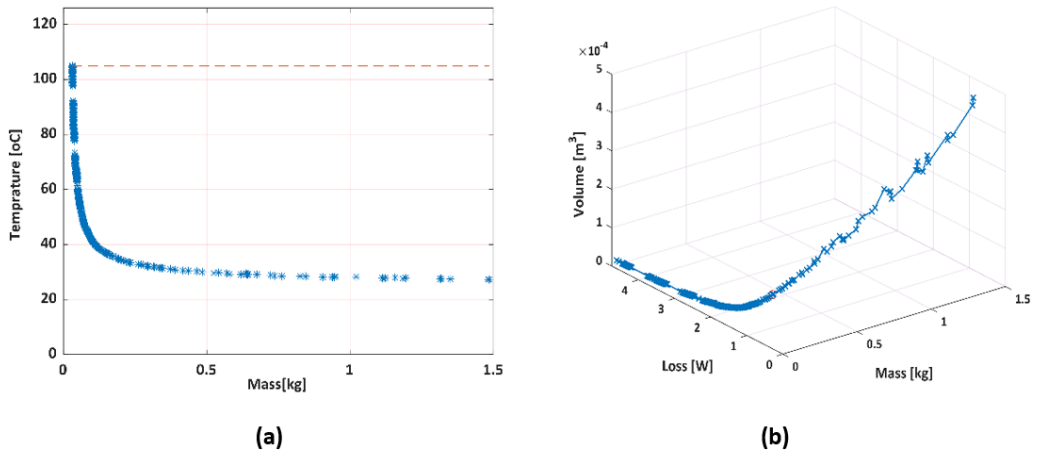

Fig. 6. The inductor's: a) maximum winding temperature versus mass; b) Pareto optimal front

Table 3. Optimal results of inductor design.

Description	Value	Description	Value
Core material	Iron powder	Axial length (height)	16.221 mm
Core mass	0.178 kg	Total core loss	0.128 W
Finished inner radius	10.012 mm	Maximum core temperature	33.634 °C
Inner core radius	12.967 mm	AWG	12
Outer core radius	28.327 mm	Total wire length	1.501 m
Outer winding radius	30.482 mm	Coil mass	0.044 kg
Conductor area	3.308 mm²	Conductor strand radius:	1.026 mm
Total mass	0.230 kg	Total volume	0.068 L
Inductance	100 µH	Resistance	3.614 mΩ

4. CONVERTER OPTIMIZATION

The optimization problem can be represented as:

$$\min_{x}\left[P_T\, V_T\right] \tag{35}$$

Subject to

$$Capacitor\ voltage\ ripple \le 1\%$$

$$Inductor\ current\ ripple \le 20\%$$

where x = [f_{sw}, C, L], f_{sw} is the switching frequency, C is capacitance values, respectively, followed by their respective inductance values L. The total volume and losses are given as

$$V_T = \left(Vol_{S,tot} + Vol_L + Vol_{C,tot}\right) \tag{36}$$

$$P_T = P_{S,tot} + P_L + P_C \tag{37}$$

where P_t is a total loss, P_L is a total inductor loss and P_C is a total capacitor loss. V_{ol} s, tot is the total switch volume, V_{olL} is the total inductor volume, and V_{olc}, tot is the total capacitor volume. Table 4, provides information on the sizes and features of passive and active components.

Table 4. Optimized converter parameter.

Device	Part selected
Capacitors (C1,2,3)	100V 2200uF
Diodes (D1)	100V @10A
MOSFETs (SW1)	100V 45A 22mΩ
Power Controller	UCC28C44DR
MPPT Controller	Raspberry Pi RP2040

5. EXPERIMENTAL PROTOTYPE

Fig. 7 illustrates the design of the developed SEPIC-Cuk converter, highlighting its main components: a power loop, a USB charger, and a control system. The majority of the converter's size and cost are detailed in Table 5.

The control system is divided into two sections: power loop feedback control and the Maximum Power Point (MPP) tracker, which incorporates the Raspberry Pi Pico controller (shown in blue) and power sampling. A cost-effective approach is employed by utilizing a dedicated integrated circuit (IC), specifically the UCCx8C4x PWM.

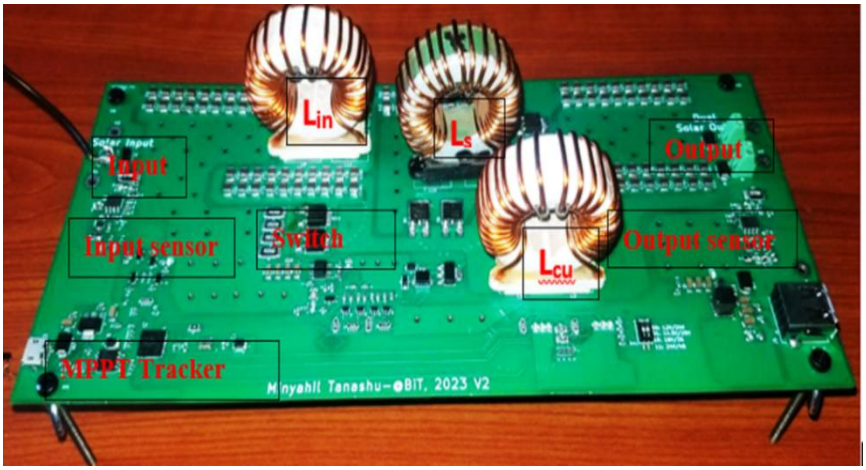

Fig. 7. The developed prototype.

6. ESTIMATED COST

The output voltage of the converter supports both 12V and 24V motors. Additionally, the converter will feature a USB output, allowing farmers and their families to charge cell phones and other small devices. Consequently, the converter should include one adjustable output for driving the electric pump and one fixed 5V output. The cost estimation for the converter is detailed in Table 5.

Table 5. Estimated cost of the converter.

Device	Part selected	Cost (per 1K parts) [$}
Capacitors (C1,2,3)	100 V, 220 µF	3 x 0.083 = 2.49
Inductors (L1,2)	100 A, 100 µH	3 x 0.13 = 0.39
Diodes (D1)	100 V, 650 mV@10A	2 x 0.079 = 0.158
MOSFETs (SW1)	100 V, 45 A, 22 mΩ	2 x 0.2 = 0.4
Power Controller	UCC28C44DR	0.53
MPPT Controller	Raspberry Pi RP2040	0.92
	Total	20 (includes all parts)

7. EXPERIMENTAL SETUP

To investigate the features and performance of a SEPIC-Cuk combination converter, an experimental prototype was developed, as illustrated in Fig. 8. The converter was designed to operate with an input voltage of 60V from a renewable energy system, providing a bipolar output of 12/24/36/48 V DC with a power rating of 300W. However, a 32V input voltage was selected for testing to account for realistic conditions and typical voltage levels encountered in solar energy systems.

Fig. 8. The experimental prototype.

8. EXPERIMENTAL RESULTS AND DISCUSSION

In Fig. 9, the reference signal for all waveforms displayed on the oscilloscope is the drain-to-source voltage of the MOSFET (shown in yellow). The second waveform represents the current flowing through inductor L1 (depicted in blue) of the SEPIC converter, while the third waveform illustrates the input voltage, which is 32V (shown in purple). In Fig. 10, the first waveform is the drain-to-source voltage (yellow), with an average value of 24V. The second waveform represents the voltage across winding L2 (blue) on the Cuk side, followed by the output voltage (purple), with measured values of 23.94V and -23.95V at the positive and negative outputs, respectively. The waveforms for the voltage across diode D1 and the output

current of the SEPIC converter, with the reference signal, are presented in Fig. 11. The output currents for the converter exhibit an average value of 9.57A, while the average output current (Io−, Io+) is 4.9A.

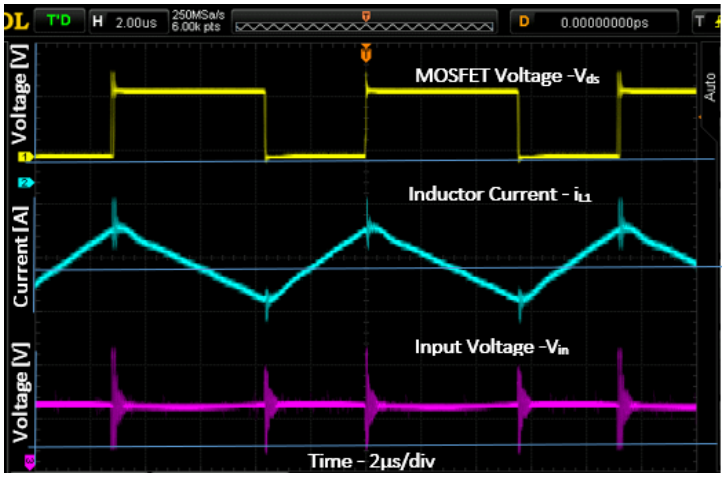

Fig. 9. Oscilloscope waveforms: MOSFET drain to source voltage, inductor (L_1) current, and input voltage, respectively.

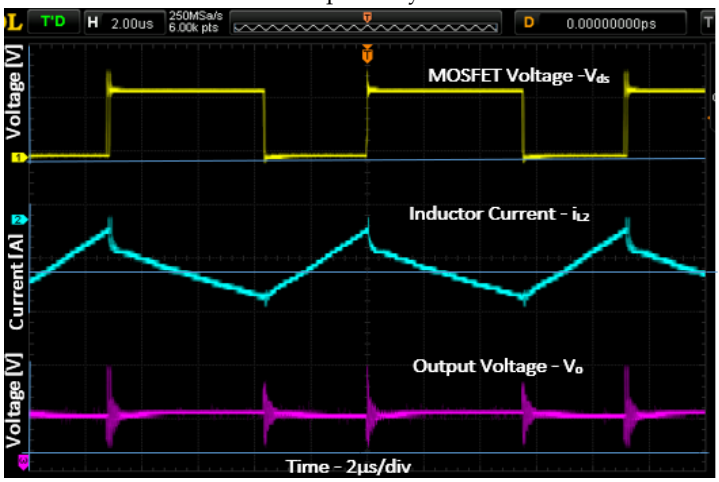

Fig. 10. Oscilloscope waveforms: MOSFET drain to source voltage, inductor (L_2) current, and output voltage, respectively.

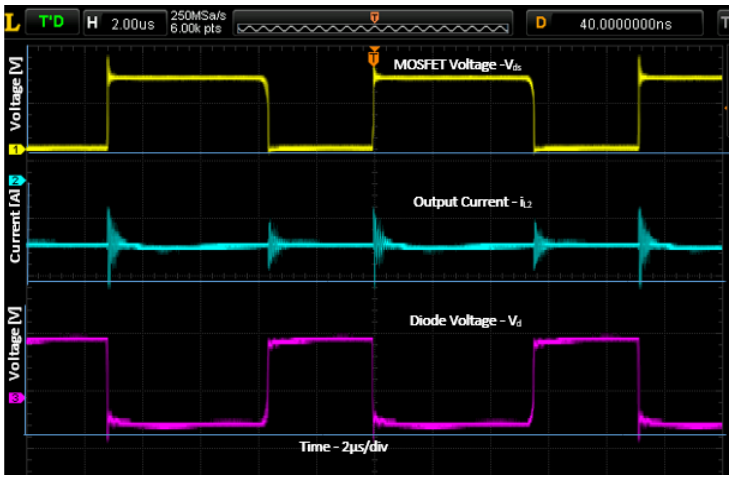

Fig. 11. Oscilloscope waveforms: MOSFET drain to source voltage, output current, and diode voltage, respectively.

Fig. 12 illustrates the relationship between output current and voltage. The output voltage reaches 24 V for a load current of 5 A. The converter delivers 300 W of power before the

load change, while the DC source provides 600 W of power. Under these conditions, with a voltage of 32 V, the average input current is 6 A.

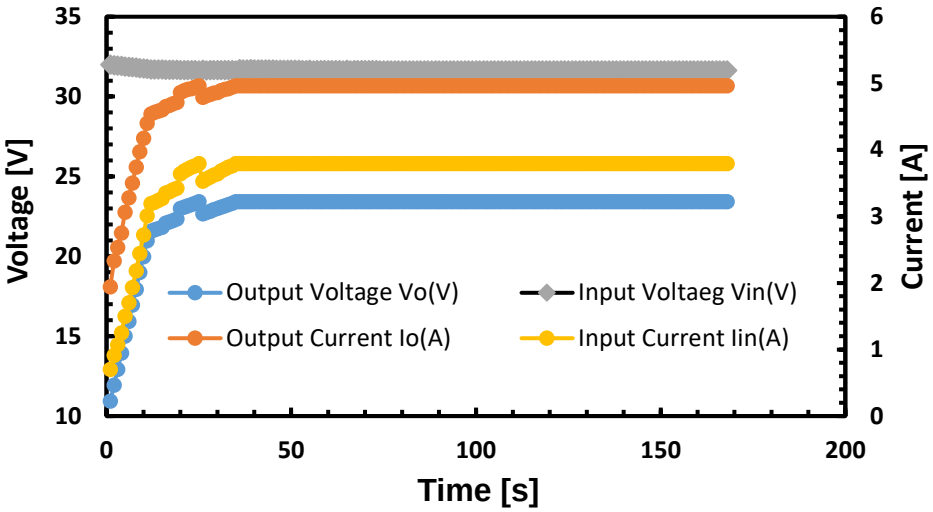

Fig. 12. The relation between input and output result.

Fig. 13 indicates that the system achieves an average efficiency of 97.5% and approximately 98.35% for a 300 W load. Existing research on DC-DC converter efficiency reports values ranging from 95% to 99%, depending on the specific application. The efficiency of commercial converters typically falls between 80% and 95%, influenced by design and application. Although compact designs are available, they often come at a higher cost or with lower power output [37-40].

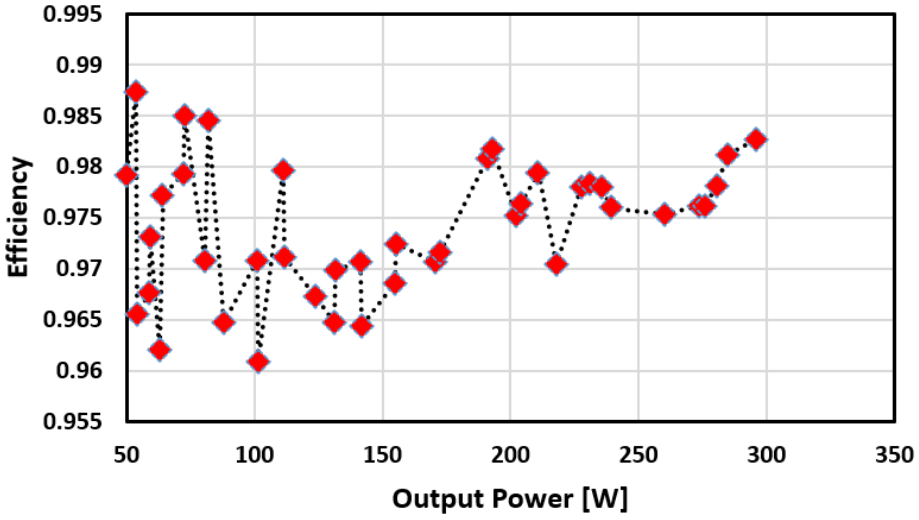

Fig. 13. The relation between measured output power and efficiency.

9. CONCLUSIONS

This research presents the development and evaluation of an experimental prototype for a single-input multiple-output (SIMO) DC-DC converter. Utilizing a SEPIC-Cuk topology, the converter generates two output voltages of equal magnitude from a single DC input. The SEPIC-Cuk combination is advantageous due to its use of only one controlled switch and a grounded control terminal, which simplifies the design compared to topologies with multiple switches. Key benefits of this converter include high efficiency, enhanced dynamic response,

and reduced ripple effects. By connecting multiple converters in parallel, losses are distributed across more components, improving thermal management and simplifying power level control with smaller output currents. Validated within a bipolar DC microgrid and distributed power system, the prototype demonstrated practical advantages in real-world settings. The study highlights the benefits of multi-objective converters in optimizing design and shows that the SEPIC-Cuk topology offers a smaller volume and reduced losses compared to traditional SEPIC and Cuk converters. Overall, this research showcases an innovative SIMO DC-DC converter that combines design simplicity with efficiency and effective thermal management. Although the prototype exhibited numerous advantages in a microgrid environment, certain issues and areas still require attention. Future studies should address the potential complexities associated with scaling the architecture for larger systems. To ensure consistent performance, further research is needed to evaluate the converter's efficiency under various load conditions. Additionally, it is essential to investigate the long-term reliability and durability of components during continuous operation to assess their lifespan and maintenance requirements. Conducting a comprehensive cost analysis is crucial for evaluating the converter's economic viability for commercial applications.

REFERENCES

[1] N. Muthukumaran, C. Kumar, R. Raj, A. Roobert, "Grey Wolf optimized PI controller for high gain SEPIC converter for PV application," International Conference on Sustainable Communication Networks and Application, 2023, doi: 10.1109/ICSCNA58489.2023.10370322.

[2] M. Khan, A. Murtaza, A. Noman, H. Sher, M. Zafar, "State-space modeling, design, and analysis of the DC-DC converters for PV application: a review," *Sustainability*, vol. 16, no. 1, p. 202, 2023, doi: 10.3390/su16010202.

[3] M. Hossain, J. Selvaraj, N. Rahim, "A novel ZVS full-bridge cascaded step-up DC-DC converter with resonant auxiliary circuit for high voltage-gain applications," *PLOS ONE,* vol. 19, no. 8, p. e0306906, 2024, doi: 10.1371/journal.pone.0306906

[4] J. Ingilala, I. Vairavasundaram, "Investigation of high gain DC/DC converter for solar PV applications," *e-Prime - Advances in Electrical Engineering, Electronics, and Energy*, vol. 5, p. 100264, 2023, doi: 10.1016/j.prime.2023.100264.

[5] H. Michael, A. Elkhateb, R. Best, "High gain isolated switched-boost DC-DC converter for PV application," IEEE Industrial and Commercial Power Systems Europe, 2023, doi: 10.1109/EEEIC/ICPSEurope57605.2023.10194620.

[6] K. Akter, S. Motakabber, A. Alam, S. Yusoff, "Design and investigation of high-power quality PV fed DC-DC boost converter," *e-Prime - Advances in Electrical Engineering, Electronics, and Energy*, vol. 9, p. 100649, 2024, doi: 10.1016/j.prime.2024.100649.

[7] S. Kumar, K. Balakrishna "A new wide input voltage DC-DC converter for solar PV systems with hybrid MPPT controller,"*Scientific Reports,* vol. 14, p. 10639, 2024, doi: 10.1038/s41598-024-61367-x.

[8] S. Jalilyan, V. Abbasi, A. Rahimi Varmenjeh, S. Ahmadian, S. Gorji, "High voltage-gain common-ground three-port DC-DC converter with low current ripples on the PV source for standalone applications," *IEEE Access*, vol. 12, pp. 80896-80909, 2024, doi: 10.1109/ACCESS.2024.3408639.

[9] T. Maniar, M. Kothari, J. Sarvaiya, M. Parmar, B. Chaudhari, D. Parmar, "Application of DC-DC converter for grid connected inverter using PV cell," *Journal of Electrical Systems,* vol. 20 , no. 7, 2024, doi: 10.52783/jes.4097

[10] S. Samiullah, K. Rachananjali, "A novel development of a new single switch inductor coupled DC-DC converter for PV system with the two-leg inverter," *Scientific Reports,* vol. 14, p. 10734, 2024, doi: 10.1038/s41598-024-61637-8

[11] D. Aeggegn, G. Nyakoe, C. Wekesa, "ANFIS-controlled boost and bidirectional buck-boost DC-DC converters for solar PV, fuel cell, and BESS-based microgrid application," *International Transactions on Electrical Energy Systems*, p. 6484369, 2024. doi: 10.1155/2024/6484369

[12] L. Fong, M. Islam, M. Ahmad, "Optimized PID controller of DC-DC buck converter based on archimedes optimization algorithm," *International Journal of Robotics and Control Systems,* vol. 3, no. 4, 2023, doi: 10.31763/ijrcs.v3i4.1113.

[13] A. Algamluoli, X. Wu, M. Mahmood, "Optimized DC-DC converter based on new interleaved switched inductor capacitor for verifying high voltage gain in renewable energy applications," *Scientific Reports*, vol. 13, p. 16436, 2023.

[14] H. Gohari, N. Mardakheh, H. Tarzamni, N. Kurdkandi, K. Abbaszadeh, J. Kyyra, "Non-isolated ultra-high voltage-gain-coupled inductor-based DC-DC converter," *IEEE Transactions on Circuits and Systems II: Express Briefs*, vol. 70, no. 12, pp. 4459 - 4463, 2023, doi: 10.1109/TCSII.2023.3285169.

[15] A. Daraz, A. Basit, G. Zhang, "Performance analysis of PID controller and fuzzy logic controller for DC-DC boost converter," *PLoS One*, vol. 18, no. 10, p. e0281122 2023, doi: 10.1371/journal.pone.0281122.

[16] S. Marlin, S. Jebaseelan, "A novel prairie dog optimization algorithm (PDOA) based MPPT controlling mechanism for grid-PV systems," *Journal of Autonomous Intelligence*, vol. 7, no. 1, 2023, doi: 10.32629/jai.v7i1.810.

[17] S. Nouri, M. Rostami, G. Kahe, "Multi-objective optimization of two-stage AC–DC power supply for reliability and efficiency using NSGA-II and meta-heuristic honeybee algorithms," *Energy Reports*, vol. 10, pp. 3174-3185, 2023, doi: 10.1016/j.egyr.2023.09.080.

[18] P. Kumari, C. Basha, F. Fathima, C. Dhanamjayulu, H. Kotb, A. ELrashidi, "Adaptive RAO ensembled dichotomy technique for the accurate parameters extraction of solar PV system," *Scientific Reports*, vol. 14, no. 1, p. 12920, 2024, doi: 10.1038/s41598-024-63383-3.

[19] H. Azaioud, A. Farnam, J. Knockaert, L. Vandevelde, J. Desmet, "Efficiency optimization and converterless PV integration by applying a dynamic voltage on an LVDC backbone," *Applied Energy*, vol. 356, p. 122416, 2024, doi: 10.1016/j.apenergy.2023.122416.

[20] G. Traiki, A. Magri, R. Lajouad, O. Bouattane, "Multi-objective control and optimization of a stand-alone photovoltaic power conversion system with battery storage energy management," *IFAC Journal of Systems and Control*, vol. 26, p. 100227, 2023, doi: 10.1016/j.ifacsc.2023.100227.

[21] M. Moradpour, P. Pirino, M. Losito, W. Franke, A. Kumar, G. Gatto, "Multi-objective optimization of the gate driver parameters in a SiC-based DC-DC converter for electric vehicles," *Energies*, vol. 13, no. 14, p. 3720, 2020, doi: 10.3390/en13143720.

[22] P. Emiliani, A. Blinov, A. Chub, G. Carne, D. Vinnikov, "DC grid interface converter based on three-phase isolated matrix topology with phase-shift modulation," International Symposium on Power Electronics for Distributed Generation Systems, 2022, doi: 10.1109/PEDG54999.2022.9923256.

[23] N. Karthik, A. Rajagopalan, M. Bajaj, P. Medhi, R. Kanimozhi, V. Blazek, L. Prokop, "Chaotic self-adaptive sine cosine multi-objective optimization algorithm to solve microgrid optimal energy scheduling problems," *Scientific Reports*, vol. 14, p. 18997, 2024, doi: 10.1038/s41598-024-69734-4.

[24] N. Hinov, B. Gilev, "Comparison of different optimization techniques for model-based design of a buck zero voltage switching quasi-resonant direct current to direct current converter," *Mathematics*, vol. 11, no. 24, p. 4990, 2023, doi: 10.3390/math11244990.

[25] S. Rodriguez; V. Rosales; O. Montero; O. Hernandez; N. Herrera; J. Sanchez, "Real-time simulation of distributed renewable energy access based on photovoltaic energy conversion system," IEEE Power & Energy Society General Meeting, 2020, doi: 10.1109/PESGM41954.2020.9281721.

[26] J. Chen, T. Tran, Y. Liu, "Design of DC micro-grid system for integration of PMSM elevator and renewable energy sources," IEEE 10th International Symposium on Power Electronics for Distributed Generation Systems, 2019, doi: 10.1109/PEDG.2019.8807695.

[27] W. Yi, D. Yi, X. Hu, X. Wang, F. Shi, "Modeling and simulation of DC micro-grid based on virtual motor control," IEEE Transportation Electrification Conference and Expo, 2017, doi: 10.1109/ITEC-AP.2017.8081004.

[28] V. Chapparya, S. Singh, A. Dey, "Novel non-isolated boost-zeta interleaved DC-DC converter for low voltage bipolar DC micro-grid application," IEEE International Conference on Power Electronics, Smart Grid, and Renewable Energy, 2022, doi: 10.1109/PESGRE52268.2022.9715812.

[29] B. Jyothi, P. Bhavana, B. Rao, M. Reddy, "A review on various DC-DC converters for photovoltaic based DC Micro grids," Emerging Trends in Industry, 2021, doi: 10.1109/ETI4.051663.2021.9619280.

[30] G. Lopez, J. Scoltock, Y. Wang, I. Laird, X. Yuan, A. Forsyth, "Power-dense bi-directional DC-DC converters with high-performance inductors," *IEEE Transactions on Vehicular Technology*, vol. 68, no. 12, pp. 11439-11448, 2019, doi: 10.1109/TVT.2019.2943124.

[31] M. Sahoo, K. Kumar, "High gain step-up DC-DC converter for DC micro-grid application," 7th International Conference on Information and Automation for Sustainability, 2014, doi: 10.1109/ICIAFS.2014.7069600.

[32] D. Eladio, L. Salvador, F. Maria, M. Moises, "DC-DC Converter with bipolar output and its use for connection of a distributed generation system to a bipolar DC grid," *Recent Advances in Electrical & Electronic Engineering*, vol. 11, no. 1, pp. 43-50, 2020, doi: 10.2174/2352096510666171108112704.

[33] H. Tacca "Core loss prediction in power electronic converters based on Steinmetz parameters," IEEE Congreso Bienal de Argentina, 2020, doi: 10.1109/ARGENCON49523.2020.9505470.

[34] V. Nascimento, S. Moon, K. Byerly, S. Sudhoff, P. Ohodnicki, "Multiobjective optimization paradigm for toroidal inductors with spatially tuned permeability," *IEEE Transactions on Power Electronics*, vol. 36, no. 3, pp. 2510-2521, 2021, doi: 10.1109/TPEL.2020.3012911.

[35] S. Hasanpour, Y. Siwakoti, F. Blaabjerg, "A new high efficiency high step-up DC/DC converter for renewable energy applications," *IEEE Transactions on Industrial Electronics*, vol. 70, no. 2, pp. 1489-1500, 2022, doi: 10.1109/TIE.2022.3161798.

[36] A. Eial Awwad, "Analysis, design, and experimental results for a high-frequency ZVZCS galvanically isolated PSFB DC-DC converter over a wide operating range using GaN-HEMT," *World Electric Vehicle Journal*, vol. 13, no. 11, p. 206, 2022, https://doi.org/10.3390/wevj13110206.

[37] A. Eial Awwad, *On the Perspectives of SiC MOSFETs in High-Frequency and High-Power Isolated DC/DC Converters*, Deutsche Nationalbibliothek, 2020.

[38] N. Blasuttigh, H. Beiranvand, T. Pereira, S. Castellan, M. Liserre, "Efficiency trade-off-oriented analysis for the integration of DC-DC converter and battery pack in V2G applications," IEEE Energy Conversion Congress and Exposition, 2022, doi: 10.1109/ECCE50734.2022.9947733.

[39] H. Mollahasanoglu, E. Ozkop "Experimental and simulated investigation of a single-phase transformerless H5 inverter topology," *Jordan Journal of Electrical Engineering*, vol. 10, no. 1, pp. 103-121, 2024, doi: 10.5455/jjee.204-1683544600.

[40] E. Can, "A common capacitor hybrid buck-boost converter," *Jordan Journal of Electrical Engineering*, vol. 9, no. 1, pp. 321-342, 2023, doi: 10.5455/jjee.204-1666615450.